10–60-GHz Electromechanical Resonators Using Thin-Film Lithium Niobate

Yansong Yang, *Member, IEEE*, Ruochen Lu, *Member, IEEE,* Liuqing Gao, *Student Member, IEEE*, and Songbin Gong, *Senior Member, IEEE*

***Abstract*— This work presents a new class of microelectromechanical system (MEMS) resonator toward 60 GHz for the fifth-generation (5G) wireless communications. The wide range of the operating frequencies is achieved by resorting to different orders of the antisymmetric Lamb wave modes in a 400-nm-thick Z-cut lithium niobate thin film. The resonance of 55 GHz demonstrated in this work marks the highest operating frequency for piezoelectric electromechanical devices. The fabricated device shows an extracted mechanical Q of 340 and an $f \times Q$ product of 1.87×10^{13} in a footprint of 2×10^{-3} mm^2. The performance has shown the strong potential of $LiNbO_3$ antisymmetric mode devices for front-end applications in 5G high-band.**

***Index Terms*— Acoustic filters, acoustic resonators, antisymmetric Lamb waves, 5G wireless communications, frequency synthesizer, Internet of Things, lithium niobate, microelectromechanical systems (MEMS).**

I. Introduction

RADIO frequency filters are indispensable components in the front ends of transceivers for selecting the input signal, improving the signal to noise ratio, avoiding spectrum growth, and duplexing transmitting (receiving) paths. They have been implemented across the entire microwave frequency range (300 MHz–30 GHz) with various technologies for addressing requirements in size, cost, weight, and performance. Recently, due to the cellular market demand for larger bandwidth (BW) and higher data rates, the sub-6-GHz spectrum has become increasingly crowded with little available spectrums for the expansion of 5G systems. As a result, 5G systems, despite varying proposed standards around the globe, have turned to millimeter-wave frequency range (24.25–40 GHz for bands n257-n260, dubbed as 5G high-band). Frequencies up to 66 GHz are currently being investigated for future releases [1], [2]. The emerging 5G systems are expected to impose stringent requirements on the size and performance of RF filters, which were not conventionally designed for handheld applications at the aforementioned frequencies.

The state-of-the-art passive RF filters that operate at room temperature and below 66 GHz can be broadly categorized into two types: electromagnetic (EM) filters or electromechanical filters. Either type can further be divided into resonant and nonresonant filters. The resonant filters rely on networking resonators for synthesizing desired frequency domain response, whereas nonresonant filters use wave propagation in structures that either have dispersion- or frequency-dependent transductions. Nonresonant filters are used in infrastructure applications, but often do not have the sharp roll-off and low insertion loss (IL) concurrently for cellular application [3]. Therefore, the focus of this work is on the building blocks of the resonant filters, namely, resonators.

TABLE I
State-of-the-Art EM Resonators and This Work

Reference	Frequency	Unloaded Q	Size
Si Cavity [9]	8-12 GHz	526	>500 mm^2
Coaxial waveguide [14]	9.9 GHz	400	>400 mm^2
Microstrip-coupled cavity [10]	10.6 GHz	448	>200 mm^2
Evanescent-mode cavity [13]	11.15 GHz	558	>240 mm^2
Si SIW [11]	30.9 GHz	341	>4 mm^2
This work	13 GHz	372	2×10^{-3} mm^2
	21.6 GHz	566	
	30.2 GHz	715	
	38.8 GHz	539	
	47.4 GHz	474	
	55.7 GHz	340	

Between the EM and electromechanical resonators, the EM resonators at RF probably have a much longer history, dating back to the early development of radar systems [4]. They resort to EM cavities that are filled with low loss dielectric materials and are bounded with reflective boundaries to confine energy and induce resonance [5]–[8]. To achieve high quality factor (Q) and low IL, the dielectric and conduction losses have been carefully managed with material selections and designs. To minimize the resonator size, the high permittivity (ε) materials with low loss tangents are preferred to reduce phase velocity and wavelength (high ε materials are typically lossy in high frequency range). However, as the unloaded Q of the small resonator is approximately proportional to the cubic root of the volume [6], small size and low loss are often not simultaneous attainable with the state of the arts (SOAs). Table I presents some representative EM resonators

Manuscript received June 18, 2020; revised September 20, 2020; accepted September 22, 2020. Date of publication October 9, 2020; date of current version December 3, 2020. This work was supported by the U.S. Defense Advanced Research Projects Agency—Microsystem Technology Office (DARPA-MTO) Near Zero Power RF and Sensor Operations (NZERO) Program *(Corresponding author: Yansong Yang.)*

The authors are with the Department of Electrical and Computing Engineering, University of Illinois at Urbana–Champaign, Urbana, IL 61801 USA (e-mail: yyang165@illinois.edu).

Color versions of one or more of the figures in this article are available online at https://ieeexplore.ieee.org.

Digital Object Identifier 10.1109/TMTT.2020.3027694

TABLE II
STATE-OF-THE-ART PIEZOELECTRIC ELECTROMECHANICAL RESONATORS

Reference	f (GHz)	Q	k_t^2	FoM	f·Q
$LiTaO_3$ SAW [22]	2	1000	7%	70	2.0×10^{12}
I.H.P SAW [24]	1.9	4000	8%	320	7.6×10^{12}
I.H.P SAW [24]	3.5	1900	8%	152	6.65×10^{12}
AlN FBAW [27]	2	3670	4.7%	172	7.34×10^{12}
AlN FBAW [27]	5.1	913	6.4%	58.4	4.56×10^{12}
ScAlN BAW [28]	3	2400	8.2%	197	7.2×10^{12}
AlN XBAW [29]	5.66	1479	10.24%	152	8.4×10^{12}
$LiNbO_3$ S0 [32]	0.5	1300	21.7%	280	0.65×10^{12}
$LiNbO_3$ SH0 [33]	0.35	2150	14.5%	365	0.75×10^{12}
$LiNbO_3$ S0 [35]	0.05	5110	30.7%	1569	0.26×10^{12}
$LiNbO_3$ A1 [37]	4.35	527	29%	153	2.3×10^{12}
$LiNbO_3$ A1 [38]	1.7	5341	6.3%	336	9.2×10^{12}
$LiNbO_3$ A1 [40]	1.65	3112	14%	435	5.1×10^{12}

with extremely high Q factors. The challenging problem with employing EM resonators for handheld applications still remains in its overly large size [9]–[14].

On the other hand, electromechanical resonators, which resort to the acoustic standing waves, have a much smaller size due to the orders of magnitude lower phase velocities of acoustic waves than EM waves. However, accessing the mechanical resonances for electrical signal processing does require an electromechanical transduction mechanism, of which the efficiency is measured by electromechanical coupling (k_t^2). The electromechanical coupling has significant implications on filter performance because the BW of a filter, regardless of its resonator composition, is fundamentally set by the interresonator coupling. In EM resonator-based filters, the coupling can be tuned exclusively in the electrical domain inductively, capacitively, or collectively with both. In contrast, the interresonator coupling of electromechanical resonator-based filters is set by both the intercoupling between resonators in the electrical domain and the electromechanical coupling (k_t^2) between electrical and mechanical domains. Whereas the former could be tuned over a wide range simply by adjusting the coupling capacitance and inductance, k_t^2 does have hard limits set by transduction mechanisms, their involved fabrication limitations, and material properties. In fact, the intercoupling between resonators is set to 1 in common electromechanical filter topologies so the BW can be maximized to the limit allowed by k_t^2. Modern electromechanical filters (seen in Table II) in the frequency range from 300 MHz to 6 GHz almost all resort to piezoelectric transduction as it offers higher k_t^2 than electrostatic, piezoresistive, and opto-electro-mechanical devices [15]–[20]. It is a predominately linear effect with insignificant second- and third-order nonlinear coefficients. Several piezoelectric materials have been extensively researched, among which aluminum nitride (AlN), lithium tantalite ($LiTaO_3$), and lithium niobate ($LiNbO_3$) have been commercially successful for enabling surface acoustic wave (SAW) and film bulk acoustic wave (FBAW or BAW) devices [21]–[29]. However, their resonances are mostly confined to below 6 GHz for several reasons. SAW devices require narrow interdigital electrodes with sub-200-nm width to scale the resonant frequencies to be over 3.5 GHz, which leads to high loss and poor power handling [25]. FBAW or BAW devices are commonly limited in the radio bands below 6 GHz as the edge effects and spurious modes are more pronounced in the higher frequency [28]. Efforts have been made to scale the FBAW device to be 30 GHz [30]. However, the thickness of AlN thin film needs to be thinned down to be 100 nm, and sub-10-nm-thin Ru is applied as the electrodes, which would produce high thermal resistance to the surrounding. Overall, significant performance compromises have to be made in scaling conventional piezoelectric resonators to be over 6 GHz.

To overcome these limitations, one alternative is to select an acoustic wave mode in a material that features large figure-of-merit (FoM $= Q \times k_t^2$) and $f \times Q$ product and can be excited in the higher order modes. Therefore, the devices with resonance scaling toward millimeter-wave frequencies can still produce reasonable FoM and $f \times Q$ product without performance compromises. Recently, several acoustic modes (S0, SH0, and A1) have been demonstrated in $LiNbO_3$ and $LiTaO_3$ with high FoM [31]–[39]. Among these acoustic wave modes, the first-order antisymmetric Lamb wave (A1) mode has been demonstrated with a record-breaking FoM of 435 in $LiNbO_3$, which marks the first time a new resonator technology with FoMs exceeds the conventional piezoelectric resonators over 1 GHz [40]. Therefore, A1 mode devices are being considered as an alternative resonator technology for sub-6-GHz applications [41]–[43]. Due to the promising performances of the A1 mode devices, higher order antisymmetric modes can be scaled up with the great performance for the resonant frequencies beyond 6 GHz [44].

In this work, we aim to extend antisymmetric Lamb wave modes in Z-cut $LiNbO_3$ thin film to higher orders for the applications up to 60 GHz. We first investigate the resonant frequencies and coupling factors of the antisymmetric modes of various orders. Next, the excitation and energy confinement of various orders are analyzed. In addition, the origins of spurious modes are identified, subsequently leading to the optimized design. Based on these studies, a film thickness of 400 nm is chosen to support the thirteenth-order antisymmetric (A13) mode up to 55 GHz, which is the highest demonstrated resonance for piezoelectric devices. The fabricated device is measured with an extracted mechanical Q of 340 at 55 GHz. This new resonator technology has shown a unique platform for front-end applications in filtering and frequency synthesis for 5G high-band.

II. ANTISYMMETRIC LAMB WAVE MODES IN LITHIUM NIOBATE THIN FILM

A. Antisymmetric Lamb Waves

Antisymmetric Lamb waves are a class of Lamb wave characterized by their antisymmetry of vibration about the median plane of the plate in which the waves are guided and propagating. Specifically, in the two sides of the median plane,

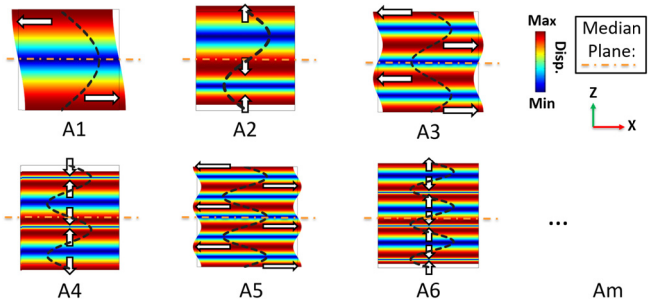

Fig. 1. Displacement mode shapes of the first-order (A1), second-order (A2), third-order (A3), fourth-order (A4), fifth-order (A5), and sixth-order (A6) antisymmetric Lamb wave modes. The arrows denote the displacement directions. The stress field for each mode order is plotted in the black dashed lines.

the vibrations of them have equal displacement components in the direction perpendicular to the median plane but different components in the direction along the median plane. To visualize the vibrations of the antisymmetric modes of various orders, COMSOL-based finite-element analysis (FEA) is used to simulate the displacement mode shapes in a 2-D Z-cut $LiNbO_3$ plate with fixed thickness where the top and bottom surfaces are set as free surfaces, and the boundary in the lateral direction is set as the infinite extent. The order of the mode is decided by the number of half-wavelength periodicities in the vertical direction, and the m^{th} order antisymmetric Lamb wave can be abbreviated as Am. Various order modes from the first (A1) to sixth (A6) are presented in Fig. 1. The stress field of each mode order is also plotted in Fig. 1. Due to the physical boundary condition for the free surfaces of the plate, the components of stress in the thickness direction at the top and bottom surfaces are zero. Clearly, overmoding the antisymmetric Lamb waves in a fixed-thickness plate would yield a higher resonant frequency, provided the intended higher order mode can somehow be excited in the $LiNbO_3$ slab with transducers.

Based on the coupling matrix of the Z-cut $LiNbO_3$ [45], antisymmetric Lamb wave modes require the electric field in the same direction of wave propagation (which is the lateral direction) to be efficiently excited, and several prior works on A1 mode have demonstrated it [46]. According to Hook's law of elasticity, to generate an acoustic wave in a piezoelectric material, the mechanical deformations and electric properties should be piezoelectrically coupled [21], [47]. The mutual energy is used to quantitatively measure the coupling between the electrical and mechanical domains

$$U_m = \frac{1}{4}\int_V (\mathrm{TdE} + \mathrm{EdT})dV \tag{1}$$

where V is the volume of the piezoelectric body, T is the stress tensor, and E is the electric strength vector. The specified acoustic wave can only be generated in the case when U_m is nonzero.

To verify the excitation of the higher order A-modes with the lateral electric field, magnitudes of the stress standing waves for different order modes are depicted based on the simulations in Fig. 1. As seen in Fig. 2, the E-field is simplified as laterally polarized with a uniform magnitude across the thickness of the plate. Thus, the integration of stress

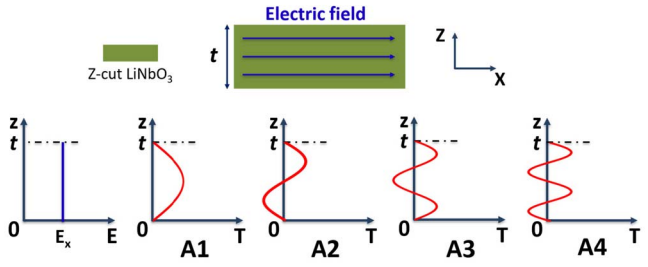

Fig. 2. Distribution of electrical and stress fields of the A1, A2, A3, and A4 modes.

and the lateral electrical fields vanish for even-order modes and lead to zero U_m. On the other hand, odd-order modes can be excited due to the nonzero integral of U_m. For the purpose of frequency scaling up to 60 GHz, our overmoding approach will focus on the odd-order modes.

B. Characteristics of A-Modes

In addition to the excitation, the resonant frequencies and electromechanical couplings of the higher odd-order A-modes need to be precisely predicted. To simplify the relationship among the resonant frequencies of different orders, the resonator body is treated as a 2-D cavity. The resonant frequency of an odd order mode in a 2-D cavity with a thickness of t and a length of l is given by [48]

$$f_0^{mn} = \sqrt{\left(\frac{mv_t}{2t}\right)^2 + \left(\frac{nv_L}{2l}\right)^2} \tag{2}$$

where m and n are the mode orders in the vertical (z-axis) and longitudinal (x-axis) directions, respectively. v_t and v_L are the acoustic velocities in the vertical and longitudinal directions. The antisymmetric modes of interest in this work have a longitudinal mode order n of 1 with a vertical mode order m that takes a value among 3, 5, 7, 9, 11, and 13. Note that (2) assumes the lateral boundaries are mechanically free, the same as the top and bottom surfaces. This assumption will be revisited later. Equation (2) also implies that any composite mode of order f_0^{mn} with n taking an odd value larger than 1 can emerge as a spurious mode near the intended mode at f_0^{m1}. Such a phenomenon has been observed for other high coupling resonators with 2-D nature [49], [50].

For modes with $n = 1$, l is equal to half of the longitudinal wavelength ($\lambda_L/2$). Thus, (2) can be rewritten as

$$f_0^{m1} = \frac{v_L}{2t}\sqrt{(\alpha m)^2 + \left(2\frac{t}{\lambda_L}\right)^2} \tag{3}$$

where α is the ratio between the velocity of vertical and longitudinal directions

$$\alpha = \sqrt{c_{44}/c_{11}}. \tag{4}$$

For the resonator in the thin-film $LiNbO_3$ slab with large wavelength ($t/\lambda_L < 0.1$), the resonant frequencies of each higher order modes can be approximated as

$$f_0^{m1} \approx \frac{v_t}{2t}m. \tag{5}$$

Clearly, the thinner $LiNbO_3$ plate would yield a higher resonant frequency for a certain order. To achieve resonant

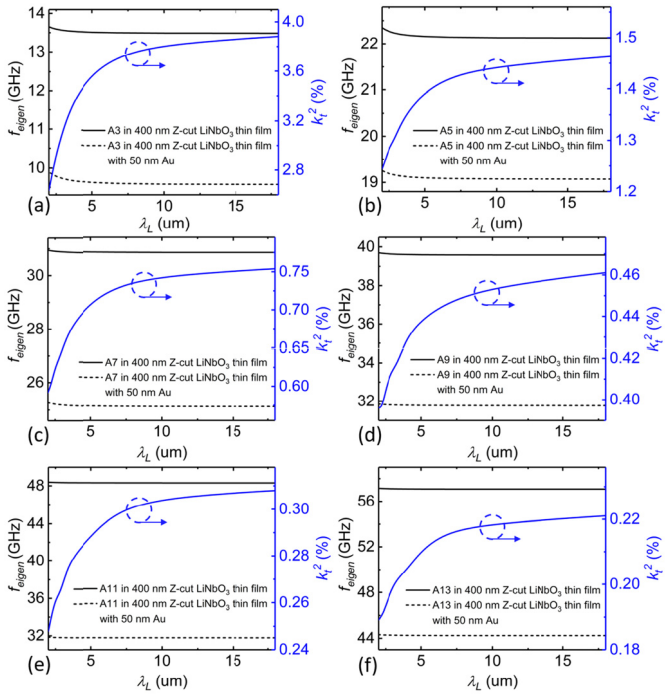

Fig. 3. Calculated dispersion and electromechanical coupling coefficients (k_t^2) of (a) A3, (b) A5, (c) A7, (d) A9, (e) A11, and (f) A13 modes.

frequency up to 60 GHz, the thickness of the $LiNbO_3$ plate is chosen to be 400 nm in this work. To validate the 2-D analysis, COMSOL-based FEA is used to calculate the eigenfrequency (f_{eigen}) variation of each odd-order A-mode in a 400-nm-thick Z-cut $LiNbO_3$ thin film. Fig. 3 shows the calculated dispersion curves of A3 to A13 modes.

In addition to the resonant frequencies, each mode is also characterized by electromechanical coupling (k_t^2) [21]

$$k_t^2 = \frac{e^2}{\varepsilon^S c^E} \cdot s_m^2 \cdot l_n^2 \tag{6}$$

where e is the piezoelectric efficient, ε^S is the permittivity under constant strain, and c^E is the stiffness under the constant electric field. s_m^2 is a scaling factor capturing the dependence of k_t^2 on the stress and electric field distributions of the mth order mode in the vertical direction. Similarly, l_n^2 represents the dependence of k_t^2 on the stress field distribution of nth order mode in the longitudinal direction, which depends on the geometry of the device. The expression of v_m^2, as part of the Berlincourt Formula, is given as

$$s_m^2 = \frac{\left(\int E_x(z)u_x(z)dz\right)^2}{\int E_x^2(z)dz \cdot \int u_x^2(z)dz}. \tag{7}$$

By using the simplified field distribution shown in Fig. 2 for integration, v_m^2 can be formulated as a function of mode order m

$$s_m^2 = \frac{1}{m^2} \tag{8}$$

l_n^2 in (7) is dependent on the ratio between the vertical and longitudinal dimensions (t/λ_L) and typically increases with respect to m. For the resonator in the thin-film $LiNbO_3$ slab with large wavelength ($t/\lambda_L < 0.1$), the

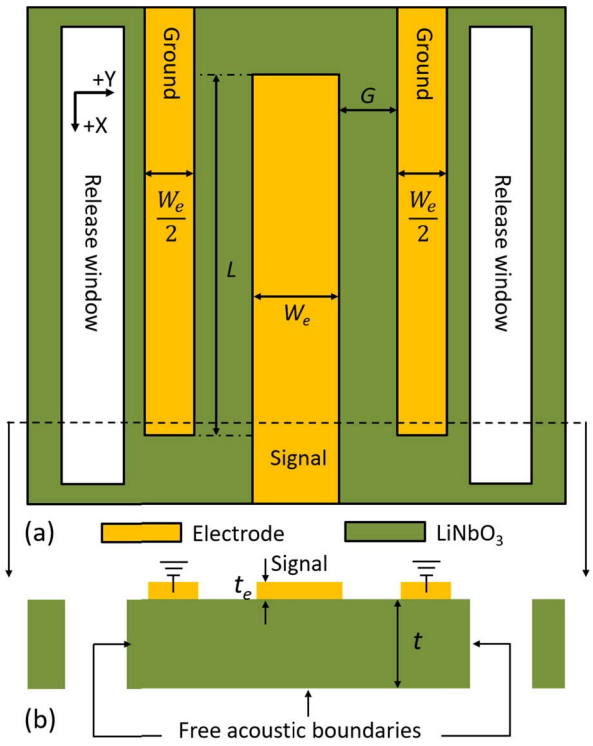

Fig. 4. (a) Top and (b) cross-sectional views of the antisymmetric mode transducer.

electromechanical coupling of each higher order modes can be approximated as

$$k_t^2 \approx \frac{e^2}{\varepsilon^S c^E} \cdot \frac{1}{m^2}. \tag{9}$$

To further understand the diminishing effect of overmoding on k_t^2 and the dispersive relationship between l_n^2 and t/λ_L, COMSOL-based FEA is used to calculate k_t^2 as a function of λ_L in a 400-nm-thick $LiNbO_3$ plate for each odd mode. As shown in Fig. 3, the results suggest that a larger λ_L (a smaller ratio of t/λ_L) leads to a larger k_t^2 for each mode and k_t^2 tends to be constant when λ_L is increased to be over 10 μm. To maximize k_t^2 in the designed device, the wavelengths of the excited modes should be over 10 μm. However, the larger wavelength leads to a larger footprint. In each specified application, the tradeoff between k_t^2 and size should be considered.

III. Design and Modeling of Antisymmetric Mode Resonators

A. Design of the Transducer

Based on the above analysis, the design of the transducer, which can generate a lateral electric field, needs to be considered. To minimize the fabrication complications, the most straightforward design is to have the interdigital electrodes patterned exclusively on top of a $LiNbO_3$ thin film. As seen in Fig. 4, the design of the transducer in this work has three interdigital electrodes connected to signal and ground, respectively, to induce lateral alternating electric fields in the mechanically suspended $LiNbO_3$ thin film. However, as described in the previous work, the electric field excited by top-only IDTs within the thin film is nonuniform, and it has

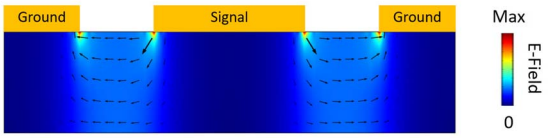

Fig. 5. FEA-simulated result of electric field distribution with electric field lines.

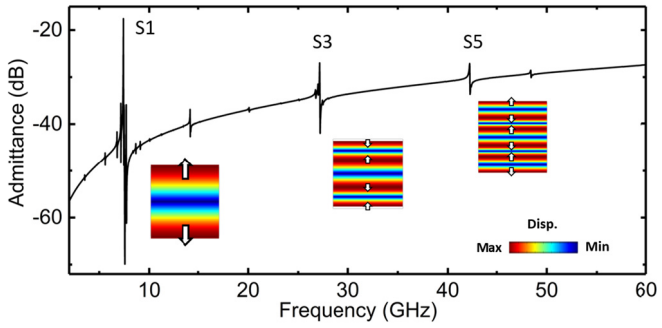

Fig. 6. Different orders of the symmetric Lamb wave modes excited by the vertical electric field in the 400-nm-thick Z-cut $LiNbO_3$ thin film.

components that can couple to the unwanted spurious modes near the A-modes [40]. As seen in Fig. 5, the FEA-simulated distribution of electric field excited by top-only IDT shows that the electric field can be decomposed into lateral and vertical components. To qualitatively understand the effect of the vertical components, an idealized vertical E-field is applied in the 400-nm-thick Z-cut $LiNbO_3$ plate. As shown in Fig. 6, the symmetric Lamb wave modes can be excited by the vertical E-field in the Z-cut $LiNbO_3$ thin film in our targeted frequency range. The displacement mode shapes of these S-modes are shown in the inset of Fig. 6. To mitigate spurious modes, the E-field distribution should be optimized based on the analysis described in our previous work on the A1 mode by using an optimal electrode gap [40].

B. Energy Confinement and Propagation Direction

In addition to the nonuniform electric field, the leakages of the acoustic waves are another origin of the unwanted spurious modes. In A1 mode devices, the spurious modes originate from insufficient confinement between electrodes in the longitudinal direction. For higher order A-modes, the acoustic energy confinement between the interdigital electrodes needs to be studied to ensure the spurious-free responses.

In addition to the spurious modes, the acoustic energy confinement also affects the quality factor of the devices. The energy confinement is more critical in the higher frequency because the acoustic losses, including damping loss of metal, often increase with the square of frequency or even worse [28], [51], [52]. To minimize the damping loss, the vibration of A-modes should be restricted in the cavity of $LiNbO_3$ between the interdigital electrodes. Therefore, the energy confinement of the higher order modes between interdigital electrodes needs to be studied to ensure a high-Q and spurious-free response. Similar to the EM waves, the confinement of acoustic waves fundamentally depends on the mismatching of the acoustic impedances between two media. As shown in Fig. 7, we approach the energy confinement by characterizing and comparing the acoustic impedance in the sections without and with electrodes. As Au is one of the densest metals with good conductivity, the electrodes made by 50-nm-thick Au is believed to generate significant mismatching of acoustic impedance, which leads to decent energy confinement. The dispersion curves of the various A-modes in the 400-nm $LiNbO_3$ plate with 50-nm Au are plotted in Fig. 3 to compare with the dispersion curves without Au. The contrast between the eigenfrequencies of each A-mode validates the energy confinement between adjacent electrodes and shows better isolation in the higher order modes.

Fig. 7. 2-D model of acoustic wave propagating in a $LiNbO_3$ plate with and without top electrodes.

In addition to the acoustic impedance mismatching, the propagation direction of the higher order modes also contributes to the better energy confinement and less spurious modes. Due to the 2-D nature, the wave vectors ($\vec{k}$) of the A-modes can be decomposed into longitudinal ($\hat{x}$) and vertical ($\hat{z}$) components

$$\vec{k} = k_l \cdot \hat{x} + k_m \cdot \hat{z} \tag{10}$$

$$k_l = \frac{2\pi}{\lambda_L} \tag{11}$$

$$\lambda_t = \frac{2t}{m} \tag{12}$$

$$k_m = \frac{2\pi}{\lambda_t} = \frac{\pi m}{t} \tag{13}$$

where k_l is the longitudinal wavenumber, k_m is the vertical wavenumber, and λ_t is the vertical wavelength. In $LiNbO_3$ thin film, k_m is much larger than k_l, and the ratio (k_m/k_l) is even higher for the higher order modes. In other words, higher order modes propagate less acoustic energy into the longitudinal direction. As stated in Section III-A, A-modes feature free boundary in the top and bottom surfaces of the $LiNbO_3$ thin film, which gives 100% energy reflection. The less longitudinal energy propagation in the higher order modes is another reason for the better energy confinement. In addition, the near-zero incidence angle at the top and bottom surfaces could help to suppress the mode conversion to mitigate spurious modes [53].

These features, different from other acoustic technologies, could lead to excellent performance in the higher frequencies (higher order modes).

C. Modeling of A-Mode Resonator

To validate resonant characteristics and spurious modes in the effects of electrodes, the resonator with the structure shown in Fig. 4 is simulated for different electrode separations. As shown in Fig. 8, the resonant frequency of each order is consistent with the analyses in Fig. 3, and most of the significant spurious modes are mitigated through increasing

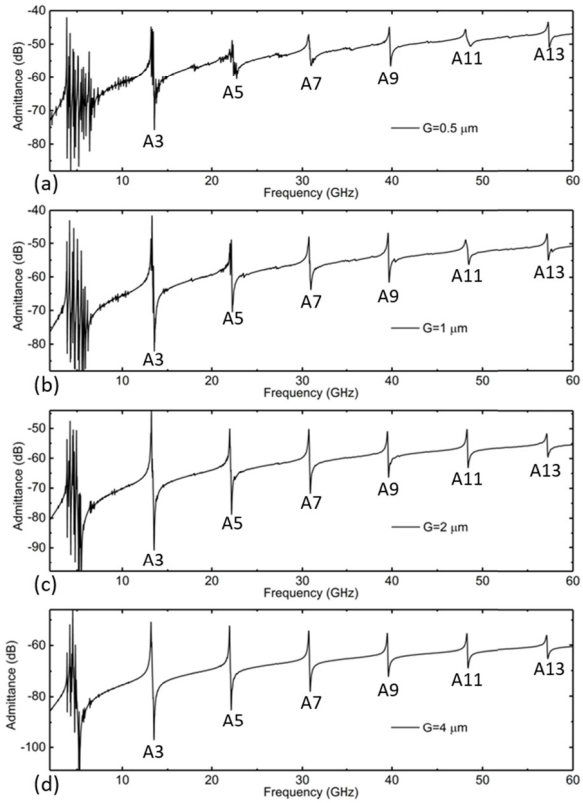

Fig. 8. FEA-simulated results of the devices with (a) $G = 0.5$ μm (b) $G = 1$ μm, (c) $G = 2$ μm, and (d) $G = 4$ μm.

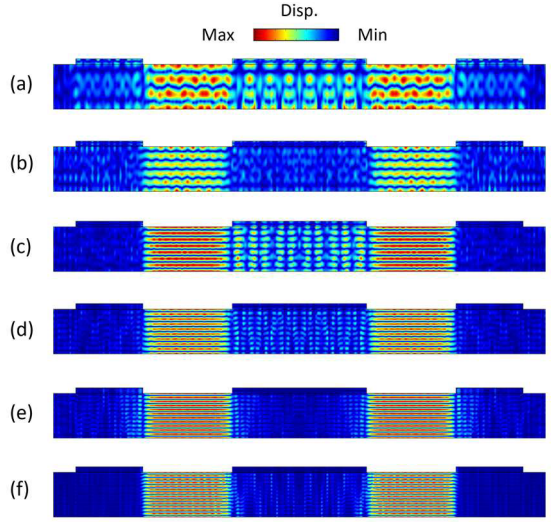

Fig. 9. FEA-simulated displacement mode shapes of (a) A3, (b) A5, (c) A7, (d) A9, (e) A11, and (f) A13 modes. The dimensions of the simulated device are listed in Table III.

the gap between interdigital electrodes from 0.5 to 4 μm due to the optimization of the electric field discussed in Section III-B.

The simulated displacement mode shapes of A3, A5, A7, A9, A11, and A13 modes are shown in Fig. 9. Consistent with our theoretical analysis of energy confinement, the FEA results show that the higher order antisymmetric modes have spurious-free responses and less acoustic energy leakage to the $LiNbO_3$ sections covered by metal.

Based on the above analyses, the thickness of the $LiNbO_3$ thin used in this work is chosen to be 400 nm, and λ_L to be 8 μm so that the A3 to A13 modes can be scaled in the frequency range from 10 to 60 GHz. The design parameters are summarized in Table III.

TABLE III
PHYSICAL DIMENSIONS OF THE DESIGNED A-MODE RESONATOR

Parameter	Description	Value
W_e	Electrode width	6 μm
G	Electrode separation	4 μm
L	Cavity length	80 μm
t	Thickness of $LiNbO_3$	400 nm
t_e	Thickness of electrode	50 nm

*The parameters are marked in Fig. 4

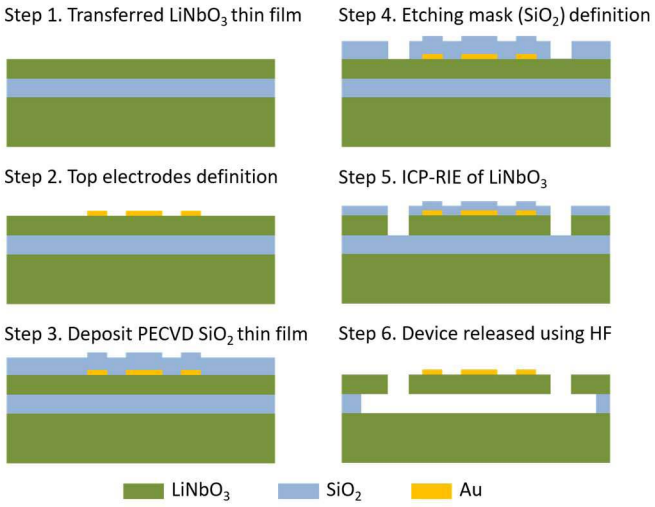

Fig. 10. Fabrication process for the $LiNbO_3$ A-mode resonator.

IV. EXPERIMENTAL RESULTS AND DISCUSSIONS

A. Fabrication of A-Mode Resonators

To validate the analytical and modeling results, the designed Z-cut $LiNbO_3$ A-mode resonator was fabricated on a 400-nm-thick Z-cut $LiNbO_3$ thin film. The fabrication process is shown in Fig. 10. A 400-nm-thick Z-cut $LiNbO_3$ thin film is transferred onto a 500-μm-thick $LiNbO_3$ carrier substrate with a thin layer of SiO_2(2 μm) as the intermediate layer. Top electrodes made for 60 nm Au are then deposited on the surface of the Z-cut $LiNbO_3$ thin film. To form the release windows shown in Fig. 4, Steps 3 to 5 are done to pattern the PECVD SiO_2 that serves as a hard mask for etching the $LiNbO_3$ thin film. The patterning of the SiO_2 and $LiNbO_3$ thin films is done in a reactive ion etching (RIE) system with inductively coupled plasma (ICP). To form the free acoustic boundaries, the SiO_2 under and on top of the $LiNbO_3$ thin film is removed through 10:1 Buffered-HF-based wet etching. As the last step after the wet etching, critical point drying (CPD) is performed to dehydrate the devices. The microscope image of the fabricated device is shown in Fig. 11. The footprint of 2×10^{-3} mm^2 can meet the most stringent size requirement of front ends.

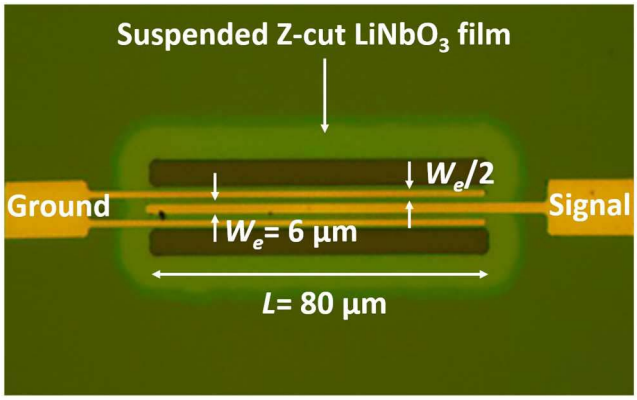

Fig. 11. Optical microscope image of the fabricated $LiNbO_3$ A-mode resonator.

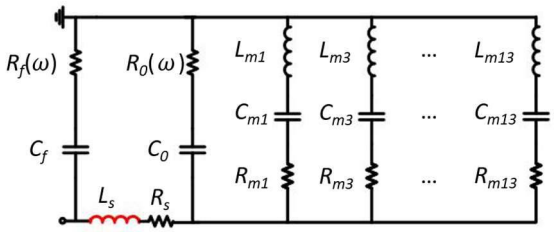

Fig. 12. Multiresonance equivalent MBVD circuit model.

The fabricated device is characterized over a wide frequency range with a Keysight N5247B PNA-X microwave network analyzer in dry air and at room temperature.

B. Admittance Response

Consistent with the simulated responses in Fig. 8, the measured responses in Fig. 13 exhibit resonant frequencies at 13, 21.6, 30.2, 38.8, 47.2, and 55.7 GHz, corresponding to the anticipated A3, A5, A7, A9, A11, and A13 modes, respectively. As expected, even-order antisymmetric Lamb wave modes cannot be excited in the device.

A multiresonance modified Butterworth-Van Dyke (MBVD) model, in which each resonance is captured by a motional branch of R_m, L_m, and C_m, is used to interpret the measurement results [44], [54], [55]. As shown in Fig. 12, an additional series inductor (L_s) is added to account for the nonnegligible inductance of the electrode fingers at high frequencies. An additional resistor (R_s) is added to account for surface resistance of electrodes and leading lines, the value of which is dependent on frequency due to skin effects. To account for the parasitic effects, C_f and R_f are included as the feedthrough capacitance and dielectric loss in the $LiNbO_3$ substrate, respectively. R_0 is added to account for the dielectric loss in the suspended $LiNbO_3$ thin film. The value of R_f and R_0 is based on the loss tangent ($\tan\delta$) of the $LiNbO_3$

$$R_f = \frac{\tan\delta}{\omega C_f} \tag{14}$$

$$R_0 = \frac{\tan\delta}{\omega C_0}. \tag{15}$$

An on-chip test structure consisting of only the bus lines was included in fabrication to measure the value of C_f.

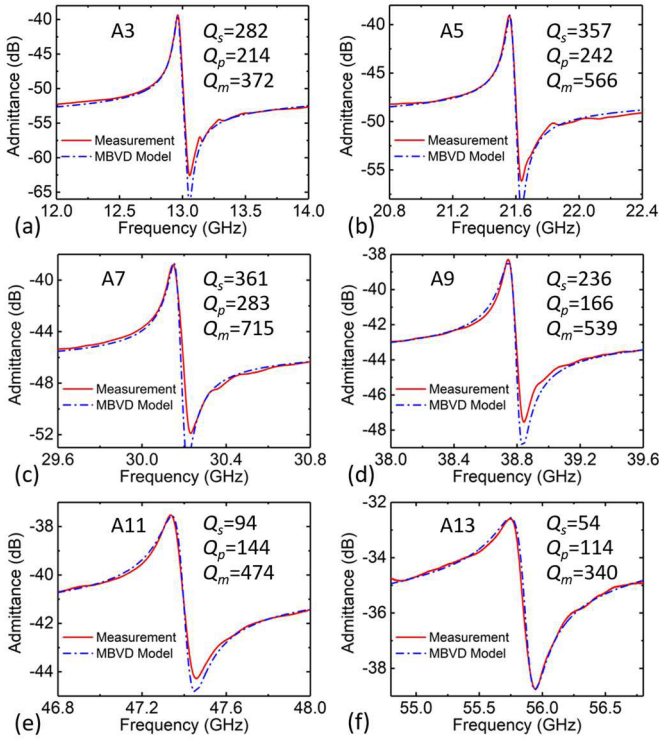

Fig. 13. Measured and MBVD modeled responses of the (a) A3, (b) A5, (c) A7, (d) A9, (e) A11, and (f) A13 modes. The parameters and measured key values are listed in Table IV.

TABLE IV
KEY MEASURED VALUES AND EXTRACTED PARAMETERS OF THE MULTIRESONANCE MBVD MODEL

Mode	A3	A5	A7	A9	A11	A13
f_0 (GHz)	13	21.6	30.2	38.8	47.4	55
R_m (Ω)	105	135	140	210	410	436
C_m (fF)	0.315	0.0964	0.0526	0.0363	0.0173	0.019
L_m (nH)	478.2	564.2	528.77	464.9	653	428.3
L_s (pH)	400	400	400	400	400	400
R_s (Ω)	12	12	13	13	14	14
C_f	10 fF					
C_0	9.3 fF					
$tan\delta$	0.007					
k_t^2	3.8%	1.2%	0.74%	0.45%	0.31%	0.22%
Q_s	282	357	361	236	94	54
Q_p	214	242	283	166	144	114
Q_m	372	566	715	539	474	340

The key parameters in the multiresonance MBVD model extracted from measurements are listed in Table IV.

C. Quality Factor

The loaded quality factor is affected by the electric and mechanical losses in $LiNbO_3$ and Au thin film [56]–[58]. Electric losses are heavily influenced by the electrode thickness. For piezoelectric-type transducers, those electrode layers scale with frequency ($1/f$) due to the mass loading effect, which leads to high resistive losses. Therefore, it is essential to use highly conductive materials with large thickness to

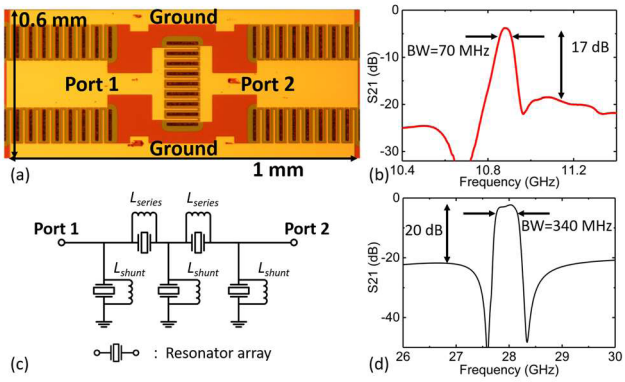

Fig. 14. (a) Optical microscope image of the fabricated A3 mode $LiNbO_3$ filter. (b) Measured response of the fabricated A-mode filter. (c) Hybrid filter topology structure. (d) Simulated response of the hybrid filter in Band n261.

keep resistive losses low. However, highly conductive metals, such as Au, often have low acoustic impedances, which directly degrade the quality factors [59]. More investigations are needed to achieve the optimized thickness of the electrodes (Au) to balance the electric and mechanical losses in electrodes. Consistent with the analysis of the energy confinements in the previous sections, the extracted mechanical Q (Q_m) of different orders decreases at a rate slower than frequency, which suggests that better energy confinements have been achieved for the higher order modes.

The dielectric loss in $LiNbO_3$ is another source of the loss affecting the admittance at antiresonance [56]. The value of the loss tangent ($\tan\delta$) is referred to the previous measurements of the dielectric properties of the single-crystal lithium niobate [60]. However, the value of $\tan\delta$ is not constant across the whole measured frequency range [61], which makes the fittings near the antiresonance not accurate for some modes. More investigations of the dielectric properties of the $LiNbO_3$ thin films are needed to understand the dielectric loss of A-modes devices at mmWave frequencies.

D. Applications of A-Mode Resonators

The demonstration of the A-mode resonators in the application of filtering is shown in Fig. 14. As the first step to scale A-mode filter toward 5G high-band, the fabricated A3 mode filter based on a 500-nm-thick $LiNbO_3$ thin film shows a footprint of 0.6 mm^2, a BW of 70 MHz, and a center frequency of 10.9 GHz. The measured result further validates the analyses on (3) that the A-mode resonances can be tuned by adjusting t and λ_L. However, due to the diminishing effect of overmoding on k_t^2, the acoustic-only A-mode filters in 5G high-band can only be used in narrowband applications.

To overcome the diminishing k_t^2 at higher-order modes, the hybrid method demonstrated at lower frequencies can be adopted for 5G high-band [54], [62]. As shown in Fig. 14(c), each resonator array is combined with a shunt inductor to compensate for the lack of adequate k_t^2. To show the feasibility of this approach, an example design for 5G NR n261 is simulated. In this example, the thickness of $LiNbO_3$ thin film is thinned down to 300 nm to attain A5 at 28 GHz with k_t^2 of 1.2%. The A5 resonance is assumed to have Q_s of 700 with future optimization. The shunt inductors are 0.45 nH and assumed to have Q of 15 at 30 GHz. As shown in Fig. 14(e), the hybrid A5 mode filter can support BW up to 340 MHz in 5G NR n261.

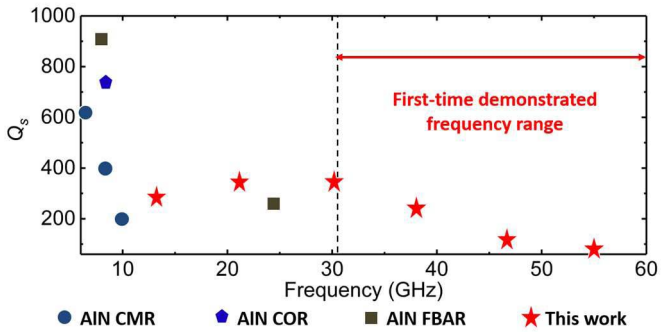

Fig. 15. Comparisons of the state-of-the-art piezoelectric electromechanical resonators above 6 GHz [30], [64]–[66].

In addition to the applications in the filtering, MEMS resonators beyond 6 GHz are also one of the vital building blocks for 5G frequency synthesizers. Based on A-mode resonators, an RF-MEMS oscillator has been primarily demonstrated with the highest reported oscillation frequency and outstanding performance [63]. Further investigations are ongoing to understand and demonstrate the potential of the A-mode resonators for front-end applications in filtering and frequency synthesis.

V. Conclusion

In this work, the antisymmetric Lamb wave modes in $LiNbO_3$ thin film have been analyzed and demonstrated in a wide range of operating frequencies. As a comparison, the loaded Q of the state-of-the-art piezoelectric electromechanical resonators operating over 6 GHz is summarized in Fig. 15 [30], [64]–[66]. The record-breaking resonant frequency of 55 GHz and the extracted mechanical Q of 340 in a fabricated device mark the first-time demonstration of the piezoelectric MEMS devices at such high frequencies. Further development and optimization of $LiNbO_3$ antisymmetric Lamb wave mode resonators could lead to miniature front-end technologies in the higher frequencies with better performance for the future wireless communication systems.

Acknowledgment

The authors thank P. Fay from the Department of Electrical Engineering at the University of Notre Dame for assistance with measurements.

References

[1] Skyworks Solutions, Inc., San Irvine, CA, USA. *5G New Radio Solutions?: Revolutionary Applications Here Sooner Than You Think*. Accessed: Nov. 5, 2019. [Online]. Available: https://www.skyworksinc.com

[2] GSMA. (2019). *5G Spectrum GSMA Public Policy Position*. Accessed: Nov. 5, 2019. [Online]. Available: https://www.gsma.com/spectrum/wp-content/uploads/2019/09/5G-Spectrum-Positions.pdf

[3] GIT. *GTI 5G Device RF Component Research Report*. Accessed: Nov. 5, 2019. [Online]. Available: http://gtigroup.org/news/gti/2019-11-22/14446.html

[4] I. Hunter, *Theory and Design of Microwave Filters*. London, U.K.: Institution Engineering Technology, 2001.

[5] X.-P. Liang and K. A. Zaki, "Modeling of cylindrical dielectric resonators in rectangular waveguides and cavities," *IEEE Trans. Microw. Theory Techn.*, vol. 41, no. 12, pp. 2174–2181, Dec. 1993.

[6] K. Wakino, T. Nishikawa, and Y. Ishikawa, "Miniaturization technologies of dielectric resonator filters for mobile communications," *IEEE Trans. Microw. Theory Techn.*, vol. 42, no. 7, pp. 1295–1300, Jul. 1994.

[7] L. Accatino, G. Bertin, and M. Mongiardo, "Elliptical cavity resonators for dual-mode narrow-band filters," *IEEE Trans. Microw. Theory Techn.*, vol. 45, no. 12, pp. 2393–2401, Dec. 1997.

[8] X.-P. Chen and K. Wu, "Substrate integrated waveguide filters: Design techniques and structure innovations," *IEEE Microw. Mag.*, vol. 15, no. 6, pp. 121–133, Sep. 2014.

[9] J. Papapolymerou, J.-C. Cheng, J. East, and L. P. B. Katehi, "A micromachined high-Q X-band resonator," *IEEE Microw. Guided Wave Lett.*, vol. 7, no. 6, pp. 168–170, Jun. 1997.

[10] M. J. Hill, R. W. Ziolkowski, and J. Papapolymerou, "A high-Q reconfigurable planar EBG cavity resonator," *IEEE Microw. Wireless Compon. Lett.*, vol. 11, no. 6, pp. 255–257, Jun. 2001.

[11] Y. Yu, Y. Zhang, and J. Zhu, "Monolithic silicon micromachined ka-band filters," in *Proc. Int. Conf. Microw. Millim. Wave Technol.*, vol. 3, Apr. 2008, pp. 1397–1400.

[12] A. Chen, A.-J.-B. J. Mousa, Y. Zhuang, Y. Huang, and J. Zhou, "Compact Ka-band substrate-integrated waveguide filter with spurlines for satellite communication systems," in *Proc. IEEE 9th U.K.-Europe-China Workshop Millimetre Waves Terahertz Technol. (UCMMT)*, Sep. 2016, pp. 10–11.

[13] A. Semnani, M. Sinanis, G. Shaffer, and D. Peroulis, "Field emission mitigation in X-band silicon-etched cavity resonators," in *IEEE MTT-S Int. Microw. Symp. Dig.*, May 2016, pp. 1–4.

[14] D. Psychogiou and K. Sadasivan, "Tunable coaxial cavity resonator-based filters using actuated liquid metal posts," *IEEE Microw. Wireless Compon. Lett.*, vol. 29, no. 12, pp. 763–766, Dec. 2019.

[15] G. Piazza, P. J. Stephanou, J. M. Porter, M. B. J. Wijesundara, and A. P. Pisano, "Low motional resistance ring-shaped contour-mode aluminum nitride piezoelectric micromeckanical resonators for UHF applications," in *Proc. 18th IEEE Int. Conf. Micro Electro Mech. Syst. (MEMS)*, Jan./Feb. 2005, pp. 20–23.

[16] K. Wang, A.-C. Wong, and C. T.-C. Nguyen, "VHF free-free beam high-Q micromechanical resonators," *J. Microelectromech. Syst.*, vol. 9, no. 3, pp. 347–360, Sep. 2000.

[17] M. Akgul, L. Wu, Z. Ren, and C. T.-C. Nguyen, "A negative-capacitance equivalent circuit model for parallel-plate capacitive-gap-transduced micromechanical resonators," *IEEE Trans. Ultrason., Ferroelectr., Freq. Control*, vol. 61, no. 5, pp. 849–869, May 2014.

[18] J. T. M. van Beek, P. G. Steeneken, and B. Giesbers, "A 10 MHz piezoresistive MEMS resonator with high Q," in *Proc. IEEE Int. Freq. Control Symp. Expo.*, Jun. 2006, pp. 475–480.

[19] J. S. Bunch *et al.*, "Electromechanical resonators from graphene sheets," *Science*, vol. 315, no. 5811, pp. 490–493, Jan. 2007.

[20] B. Chitara and A. Ya'akobovitz, "High-frequency electromechanical resonators based on thin GaTe," *Nanotechnology*, vol. 28, no. 42, Oct. 2017, Art. no. 42LT02.

[21] K. Hashimoto, *RF Bulk Acoustic Wave Filters for Communications*. Norwood, MA, USA: Artech House, 2009.

[22] T. Kimura, M. Kadota, and Y. Ida, "High Q SAW resonator using upper-electrodes on grooved-electrodes in $LiTaO_3$," in *IEEE MTT-S Int. Microw. Symp. Dig.*, May 2010, pp. 1740–1743.

[23] K. Hashimoto, *Surface Acoustic Wave Devices in Telecommunications*. Berlin, Germany: Springer, 2000.

[24] T. Takai *et al.*, "I.H.P. SAW technology and its application to microacoustic components (Invited)," in *Proc. IEEE Int. Ultrason. Symp. (IUS)*, Sep. 2017, pp. 1–8.

[25] T. Kimura, M. Omura, Y. Kishimoto, and K. Hashimoto, "Comparative study of acoustic wave devices using thin piezoelectric plates in the 3–5-GHz range," *IEEE Trans. Microw. Theory Techn.*, vol. 67, no. 3, pp. 915–921, Mar. 2019.

[26] H. P. Loebl, M. Klee, C. Metzmacher, W. Brand, R. Milsom, and P. Lok, "Piezoelectric thin AlN films for bulk acoustic wave (BAW) resonators," *Mater. Chem. Phys.*, vol. 79, nos. 2–3, pp. 143–146, Apr. 2003.

[27] R. Ruby *et al.*, "Positioning FBAR technology in the frequency and timing domain," *IEEE Trans. Ultrason., Ferroelectr., Freq. Control*, vol. 59, no. 3, pp. 334–345, Mar. 2012.

[28] R. Aigner, G. Fattinger, M. Schaefer, K. Karnati, R. Rothemund, and F. Dumont, "BAW filters for 5G bands," in *IEDM Tech. Dig.*, Dec. 2018, pp. 14.5.1–14.5.5.

[29] Y. Shen, P. Patel, R. Vetury, and J. B. Shealy, "452 MHz bandwidth, high rejection 5.6 GHz UNII XBAW coexistence filters using doped AlN-on-Silicon," in *IEDM Tech. Dig.*, Dec. 2019, vol. 5, no. 6, pp. 1–4.

[30] M. Hara *et al.*, "Super-high-frequency band filters configured with air-gap-type thin-film bulk acoustic resonators," *Jpn. J. Appl. Phys.*, vol. 49, no. 7, Jul. 2010, Art. no. 07HD13.

[31] S. Gong and G. Piazza, "Design and analysis of lithium–niobate-based high electromechanical coupling RF-MEMS resonators for wide-band filtering," *IEEE Trans. Microw. Theory Techn.*, vol. 61, no. 1, pp. 403–414, Jan. 2013.

[32] S. Gong and G. Piazza, "Figure-of-merit enhancement for laterally vibrating lithium niobate MEMS resonators," *IEEE Trans. Electron Devices*, vol. 60, no. 11, pp. 3888–3894, Nov. 2013.

[33] R. H. Olsson *et al.*, "A high electromechanical coupling coefficient SH0 Lamb wave lithium niobate micromechanical resonator and a method for fabrication," *Sens. Actuators A, Phys.*, vol. 209, pp. 183–190, Mar. 2014.

[34] R. Wang, S. A. Bhave, and K. Bhattacharjee, "Design and fabrication of S0 Lamb-wave thin-film lithium niobate micromechanical resonators," *J. Microelectromech. Syst.*, vol. 24, no. 2, pp. 300–308, Apr. 2015.

[35] L. Colombo, A. Kochhar, G. Vidal-Alvarez, and G. Piazza, "X-cut lithium niobate laterally vibrating MEMS resonator with figure of merit of 1560," *J. Microelectromech. Syst.*, vol. 27, no. 4, pp. 602–604, Aug. 2018.

[36] M. Kadota, T. Ogami, K. Yamamoto, and H. Tochishita, "LiNbO3 thin film for a1 mode of Lamb wave resonators," *Phys. Status Solidi A*, vol. 208, no. 5, pp. 1068–1071, May 2011.

[37] Y. Yang, A. Gao, R. Lu, and S. Gong, "5 GHz lithium niobate MEMS resonators with high FoM of 153," in *Proc. IEEE 30th Int. Conf. Micro Electro Mech. Syst. (MEMS)*, Jan. 2017, pp. 942–945.

[38] Y. Yang, R. Lu, T. Manzaneque, and S. Gong, "1.7 GHz Y-cut lithium niobate MEMS resonators with FoM of336 andfQ of9.15×10^{12}," in *IEEE MTT-S Int. Microw. Symp. Dig.*, Jun. 2018, pp. 563–566.

[39] V. Plessky, S. Yandrapalli, P. J. Turner, L. G. Villanueva, J. Koskela, and R. B. Hammond, "5 GHz laterally-excited bulk-wave resonators (XBARs) based on thin platelets of lithium niobate," *Electron. Lett.*, vol. 55, no. 2, pp. 98–100, Jan. 2019.

[40] Y. Yang, R. Lu, and S. Gong, "A 1.65 GHz lithium niobate a1 resonator with electromechanical coupling of 14% and Q of 3112," in *Proc. IEEE 32nd Int. Conf. Micro Electro Mech. Syst. (MEMS)*, Jan. 2019, pp. 875–878.

[41] Y. Yang, R. Lu, L. Gao, and S. Gong, "4.5 GHz lithium niobate MEMS filters with 10% fractional bandwidth for 5G front-ends," *J. Microelectromech. Syst.*, vol. 28, no. 4, pp. 575–577, Aug. 2019.

[42] R. Lu, Y. Yang, M.-H. Li, M. Breen, and S. Gong, "5-GHz antisymmetric mode acoustic delay lines in lithium niobate thin film," *IEEE Trans. Microw. Theory Techn.*, vol. 68, no. 2, pp. 573–589, Feb. 2020.

[43] P. J. Turner *et al.*, "5 GHz band n79 wideband microacoustic filter using thin lithium niobate membrane," *Electron. Lett.*, vol. 55, no. 17, pp. 942–944, Aug. 2019.

[44] Y. Yang, R. Lu, T. Manzaneque, and S. Gong, "Toward Ka band acoustics: Lithium niobate asymmetrical mode piezoelectric MEMS resonators," in *Proc. IEEE Int. Freq. Control Symp. (IFCS)*, May 2018, pp. 1–5.

[45] K. K. Wang, *Properties of Lithium Niobate*. London, U.K.: INSPEC, 2002.

[46] Y. Yang, R. Lu, and S. Gong, "High *Q* antisymmetric mode lithium niobate MEMS resonators with spurious mitigation," *J. Microelectromech. Syst.*, vol. 29, no. 2, pp. 135–143, Apr. 2020.

[47] A. C. Ugural and S. K. Fenster, *Advanced Strength and Applied Elasticity*. London, U.K.: Pearson Education, 2003.

[48] J. F. Rosenbaum, *Bulk Acoustic Wave Theory and Devices*. Norwood, MA, USA: Artech House, 1988.

[49] C. Cassella, Y. Hui, Z. Qian, G. Hummel, and M. Rinaldi, "Aluminum nitride cross-sectional Lamé mode resonators," *J. Microelectromech. Syst.*, vol. 25, no. 2, pp. 275–285, Apr. 2016.

[50] Y.-H. Song, R. Lu, and S. Gong, "Analysis and removal of spurious response in SH0 lithium niobate MEMS resonators," *IEEE Trans. Electron Devices*, vol. 63, no. 5, pp. 2066–2073, May 2016.

[51] W. P. Mason and H. J. McSkimin, "Attenuation and scattering of high frequency sound waves in metals and glasses," *J. Acoust. Soc. Amer.*, vol. 19, no. 3, pp. 464–473, May 1947.

[52] W. P. Mason and H. J. McSkimin, "Energy losses of sound waves in metals due to scattering and diffusion," *J. Appl. Phys.*, vol. 19, no. 10, pp. 940–946, Oct. 1948.

[53] B. A. Auld, *Acoustic Fields and Waves in Solids*. Moscow, Russia: Ripol Classic, 1973.

[54] D. Psychogiou, R. Gomez-Garcia, R. Loeches-Sanchez, and D. Peroulis, "Hybrid acoustic-wave-lumped-element resonators (AWLRs) for high-*Q* bandpass filters with quasi-elliptic frequency response," *IEEE Trans. Microw. Theory Techn.*, vol. 63, no. 7, pp. 2233–2244, Jul. 2015.
[55] R. Lu, M.-H. Li, Y. Yang, T. Manzaneque, and S. Gong, "Accurate extraction of large electromechanical coupling in piezoelectric MEMS resonators," *J. Microelectromech. Syst.*, vol. 28, no. 2, pp. 209–218, Apr. 2019.
[56] J. D. Larson, P. D. Bradley, S. Wartenberg, and R. C. Ruby, "Modified Butterworth-Van Dyke circuit for FBAR resonators and automated measurement system," in *Proc. IEEE Ultrason. Symp.*, vol. 1, Oct. 2000, pp. 863–868.
[57] J. Bjurstrom, L. Vestling, J. Olsson, and I. Katardjiev, "An accurate direct extraction technique for the MBVD resonator model," in *Proc. 34th Eur. Microw. Conf.*, vol. 3, Oct. 2004, pp. 1241–1244.
[58] G. Piazza, P. J. Stephanou, and A. P. Pisano, "Piezoelectric aluminum nitride vibrating contour-mode MEMS resonators," *J. Microelectromech. Syst.*, vol. 15, no. 6, pp. 1406–1418, Dec. 2006.
[59] M. Schaefer, R. Rothemund, and G. Fattinger, "Process and design challenge for SMR-type bulk acoustic wave (BAW) filters at frequencies above 5 GHz," in *Proc. IEEE Int. Ultrason. Symp. (IUS)*, Oct. 2019, pp. 1696–1699.
[60] R. T. Schermer *et al.*, "Millimeter-wave dielectric properties of highly refractive single crystals characterized by waveguide cavity resonance," *Adv. Mater. Interfaces*, vol. 67, no. 3, pp. 1–36, 2019.
[61] J. S. Mccloy, K. A. Korolev, Z. Li, M. N. Afsar, and S. K. Sundaram, "Millimeter-wave dielectric properties of single-crystal ferroelectric and dielectric materials," *IEEE Trans. Ultrason., Ferroelectr., Freq. Control*, vol. 58, no. 1, pp. 18–29, Jan. 2011.
[62] C. Zuo, C. He, W. Cheng, and Z. Wang, "Hybrid filter design for 5G using IPD and acoustic technologies," in *Proc. IEEE Int. Ultrason. Symp. (IUS)*, Oct. 2019, pp. 1–4.
[63] A. Kourani, Y. Yang, and S. Gong, "A Ku-band oscillator utilizing overtone lithium niobate RF-MEMS resonator for 5G," *IEEE Microw. Wireless Compon. Lett.*, vol. 30, no. 7, pp. 681–684, Jul. 2020.
[64] E. Iborra, M. Clement, J. Capilla, J. Olivares, and V. Felmetsger, "Optimization of thin AlN sputtered films for X-band BAW resonators," in *Proc. IEEE Int. Ultrason. Symp.*, Oct. 2010, pp. 1688–1691.
[65] M. Rinaldi, C. Zuniga, and G. Piazza, "5-10 GHz AlN contour-mode nanoelectromechanical resonators," in *Proc. IEEE 22nd Int. Conf. Micro Electro Mech. Syst.*, Jan. 2009, pp. 916–919.
[66] G. Chen and M. Rinaldi, "High-Q X band aluminum nitride combined overtone resonators," in *Proc. Joint Conf. IEEE Int. Freq. Control Symp. Eur. Freq. Time Forum (EFTF/IFC)*, Apr. 2019, pp. 1–3.

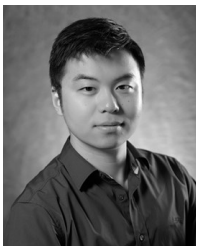

Yansong Yang (Member, IEEE) received the B.S. degree in electrical and electronic engineering from the Huazhong University of Science and Technology, Wuhan, China, in 2014, and the M.S. and Ph.D. degrees in electrical engineering from the University of Illinois at Urbana–Champaign, Urbana, IL, USA, in 2017 and 2019, respectively.

He is currently a Post-Doctoral Researcher with the University of Illinois at Urbana–Champaign. His research interests include design and microfabrication techniques of RF MEMS resonators, filters, switches, and photonic integrated circuits.

Dr. Yang has won the Second Place in Best Paper Competition at the 2018 IEEE International Microwave Symposium, and the Best Paper Award at the 2019 IEEE International Ultrasonics Symposium. He was also a Finalist for the Best Paper Award at the 2018 IEEE International Frequency Control Symposium. He was also a recipient of the 2019 P. D. Coleman Graduate Research Award from the Department of Electrical and Computer Engineering at UIUC.

Ruochen Lu (Member, IEEE) received the B.E. degree (Hons.) in microelectronics from Tsinghua University, Beijing, China, in 2014, and the M.S. and Ph.D. degrees in electrical engineering from the University of Illinois at Urbana–Champaign (UIUC), Urbana, IL, USA, in 2017 and 2019, respectively.

He is currently a Post-Doctoral Researcher with UIUC. He will join the Department of Electrical and Computer Engineering, The University of Texas at Austin, Austin, TX, USA, as an Assistant Professor, in January 2021. His research interest includes radio frequency microsystems and their applications for timing and signal processing.

Dr. Lu received the Best Student Paper Awards at the 2017 IEEE International Frequency Control Symposium, the 2018 IEEE International Ultrasonics Symposium, the 2015 Lam Graduate Award, the 2017 Nick Holonyak, the Jr. Graduate Research Award, the 2018 Nick Holonyak, the Jr. Fellowship, and the 2019 Raj Mittra Outstanding Research Award from the Department of Electrical and Computer Engineering at UIUC.

Liuqing Gao (Student Member, IEEE) received the B.S. and M.S. degrees in electrical engineering from the University of Illinois at Urbana–Champaign, Urbana, IL, USA, in 2016 and 2020, respectively, where she is currently pursuing the Ph.D. degree.

Her research interests include design and microfabrication techniques of MEMS resonators, filters, and wireless communication systems.

Mrs. Gao has won the Best Student Paper Award at 2020 IEEE International Ultrasonics Symposium, and the third place in Best Paper Competition at 2020 IEEE International Microwave Symposium. She was also a recipient of the 2015 Omron Electrical Engineering Scholarship, the 2016 E. C. Jordan Awards, the 2016 Illinois Engineering Achievement Scholarship, the 2016 Highest Honors at Graduation, the 2017 ECE Distinguished Research Fellowship, the 2018 James M. Henderson Fellowship, the 2019 Dr. Ok Kyun Kim Fellowship, and the 2020 John Bardeen Graduate Research Award from the Department of Electrical and Computer Engineering at UIUC.

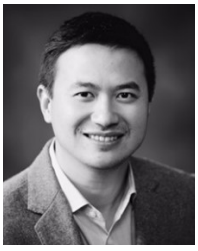

Songbin Gong (Senior Member, IEEE) received the Ph.D. degree in electrical engineering from the University of Virginia, Charlottesville, VA, USA, in 2010.

He is currently an Associate Professor and the Intel Alumni Fellow with the Department of Electrical and Computer Engineering and the Micro and Nanotechnology Laboratory, University of Illinois at Urbana–Champaign, Urbana, IL, USA. His research primarily focuses on design and implementation of radio frequency microsystems, components, and subsystems for reconfigurable RF front ends. In addition, his research explores hybrid microsystems based on the integration of MEMS devices with photonics or circuits for signal processing and sensing.

Dr. Gong was a recipient of the 2014 Defense Advanced Research Projects Agency Young Faculty Award, the 2017 NASA Early Career Faculty Award, the 2019 UIUC College of Engineer Dean's Award for Excellence in Research, and the 2019 Ultrasonics Early Career Investigator Award. Along with his students and postdocs, he received the Best Paper Awards from the 2017 and 2019 IEEE International Frequency Control Symposium, the 2018 and 2019 International Ultrasonics Symposium, and won second place in Best Paper Competition at the 2018 IEEE International Microwave Symposium. He is a Technical Committee Member of MTT-21 RF-MEMS of the IEEE Microwave Theory and Techniques Society, the International Frequency Control Symposium, and the International Electron Devices Meeting, and currently serves as the Chair of MTT TC2 and TC 21, and an Associate Editor for T-UFFC and JMEMS.